

## Article

# A New Shear Constitutive Model Characterized by the Pre-Peak Nonlinear Stage

Shijie Xie <sup>1,2</sup>, Hang Lin <sup>2</sup>, Zhenyu Han <sup>1,3,\*</sup>, Hongyu Duan <sup>4</sup>, Yifan Chen <sup>2,\*</sup> and Diyuhan Li <sup>2</sup><sup>1</sup> School of Civil Engineering, Southeast University, Nanjing 210096, China<sup>2</sup> School of Resources and Safety Engineering, Central South University, Changsha 410083, China<sup>3</sup> Department of Civil Engineering, Monash University, Melbourne, VIC 3800, Australia<sup>4</sup> Discipline of Civil, Surveying & Environmental Engineering, School of Engineering, University of Newcastle, Callaghan, NSW 2308, Australia

\* Correspondence: zhenyu\_han@seu.edu.cn (Z.H.); 185506005@csu.edu.cn (Y.C.)

**Abstract:** The pre-peak shear stress-displacement curve is an important part of the study of the shear mechanical behavior of rock joints. Underpinned by the Haldane distribution, a new semi-analytical model for the pre-peak shear deformation of rock joints was established in this paper, the validity of which was verified by laboratory and in situ experimental data. Other existing models were employed to make comparisons. The comparison results show that the model has superior adaptability and is more suitable for convex-type shear constitutive curves than existing models. Besides, only one parameter was introduced to the model, which is more convenient for application. All of these imply that the proposed model is an effective tool to evaluate the pre-peak shear constitutive curves of different rock joints. The research results can provide a reference for further understanding of the shear fracture characteristics of rock materials.

**Keywords:** fracture characteristics; rock joint; pre-peak shear constitutive curve; shear deformation evolution



**Citation:** Xie, S.; Lin, H.; Han, Z.; Duan, H.; Chen, Y.; Li, D. A New Shear Constitutive Model Characterized by the Pre-Peak Nonlinear Stage. *Minerals* **2022**, *12*, 1429. <https://doi.org/10.3390/min12111429>

Academic Editor: Gianvito Scaringi

Received: 10 October 2022

Accepted: 3 November 2022

Published: 10 November 2022

**Publisher's Note:** MDPI stays neutral with regard to jurisdictional claims in published maps and institutional affiliations.



**Copyright:** © 2022 by the authors. Licensee MDPI, Basel, Switzerland. This article is an open access article distributed under the terms and conditions of the Creative Commons Attribution (CC BY) license (<https://creativecommons.org/licenses/by/4.0/>).

## 1. Introduction

The intact rock masses in nature are cut by rock joints into rock blocks, forming jointed rock masses as shown in Figure 1 [1,2]. The failure of rock joints dominates more than that of rock blocks during the instability of jointed rock masses [3,4]. Most geotechnical engineering projects are usually constructed in jointed rock masses [5], and the shear mechanical properties of rock joints are one of the main factors controlling the mechanical stability of underground excavations [6]. For example, it has been reported that the collapse of the São Paulo metro station in Brazil may be related to an over-simplified geomechanical model used in the engineering design process [7]. Therefore, understanding the shear deformation behavior of rock joints is very important for the safety assessment of geoengineering structures (such as rock slopes, tunnels, dam foundations, chambers, and waste repositories) [8,9].

Rock materials are a complex mineral aggregate formed under physical and chemical actions after a long geological process [10–12], which makes the link between stress and strain (or displacement) of rock materials has been one of the most pressing issues over the past decades [13]. Extensive theoretical analysis, experimental tests, and numerical simulation studies have been implemented at the laboratory scale on the shear deformation behavior of rock joints, and fruitful results have been obtained [14–20]. It mainly includes the research on shear strength [21,22], shear constitutive models [23,24], surface failure characteristics [25–28], as well as the influencing laws of rock type [29], boundary conditions [30] and loading mode [31], and other factors. Jing [32] and Muralha et al. [33] provide an admirable summary of the suggested method for laboratory shear tests of rock joints and the importance of rock joints in understanding rock mechanics for a variety of

engineering applications. The shear stress/shear displacement curve is one of the most important considerations to evaluate the shear mechanical properties of rock joints [34]. Nonetheless, it is still difficult to establish a constitutive model that can fully reflect the shear stress/shear displacement curve behavior of joint materials, especially considering the complex nonlinear mechanical properties of joint materials [35,36]. Among the aforementioned pioneering studies, it is fully recognized that the shear stress/shear displacement curve of the rock sample subjected to shear tests can be divided by peak points into two critical stages, the pre-peak stage and post-peak stage. Because the shear test requires specific test conditions, the test results themselves have a certain discreteness [37]. In practice, it is difficult to select the most suitable test results to evaluate the shear constitutive relationship [38], and the shear stress/shear displacement curve is essential to describe the shear fracture characteristics of rock joints [39]. According to the classical failure curve of rock joints [40,41], except for peak stress, the stress thresholds of crack compaction, crack initiation and rock damage are all located in the pre-peak stage, which is closely associated with crack development. However, there are rare reports on the pre-peak stress and deformation characteristics [42]. Therefore, it is still necessary to study the theoretical modeling of pre-peak shear stress/shear displacement curves of rock joints.

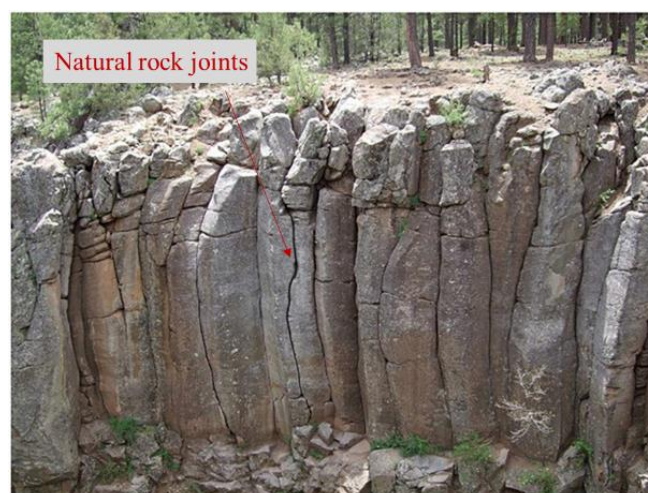


**Figure 1.** Example of jointed rock mass(modified after [1]).

Modeling studies to investigate the pre-peak shear stress- displacement curve of rock joints began in the late 1960s and early 1970s. Goodman [43] and Saeb et al. [44] regarded the pre-peak shear stress/shear displacement curve as quasi-linear and used linear functions to characterize the pre-peak shear stress- shear displacement curve of rock joints. Obviously, this oversimplification cannot describe the nonlinear deformation characteristics in the pre-peak stage. Based on a series of direct shear tests, Kulhawy [45] first proposed a hyperbolic function to describe the nonlinear pre-peak shear stress- displacement relationship. Subsequently, referring to the work of Kulhawy [45], Bandis et al. [46] proposed a hyperbolic model to fit the pre-peak shear stress-shear displacement curve and verified the applicability of this model by comparing it with some existing test results. Under the framework of plasticity theory, Desai and Fishman [47] established a pre-peak constitutive model to simulate joints under monotonic loading, unloading and reverse loading. Nassir et al. [48] further generalized the Bandis model [46] by introducing the dilation initiation coefficient to characterize the fraction of peak shear displacement at which dilation initiates, and then calibrated the model based on experimental results. Inspired by the idea of normalization, Ban et al. [49] made the shear stiffness dimensionless and established a hyperbolic shear constitutive considering shear stiffness softening to describe the pre-peak shear stress/shear displacement curve. Kou et al. [50] also studied the pre-peak shear behavior of rock joints contain the triangular-shaped primary and subordinated asperities through pre-peak cyclic shear test. Despite those models inspiring the research on the

characterization of pre-peak shear constitutive curves, they only accord well with curves with specific morphology (i.e., the concave-type curve in Figure 2). Shen et al. [51] pointed out that the pre-peak shear stress curves of many joints presents a convex-type shear constitutive curve (i.e., convex-type curve). However, due to the limitation of hyperbolic function itself, the hyperbolic models mentioned above cannot represent this convex-type curve. In fact, there is currently no model that can simultaneously represent the three types of pre-peak shear curves shown in Figure 2. Therefore, it is necessary to carry out in-depth research.

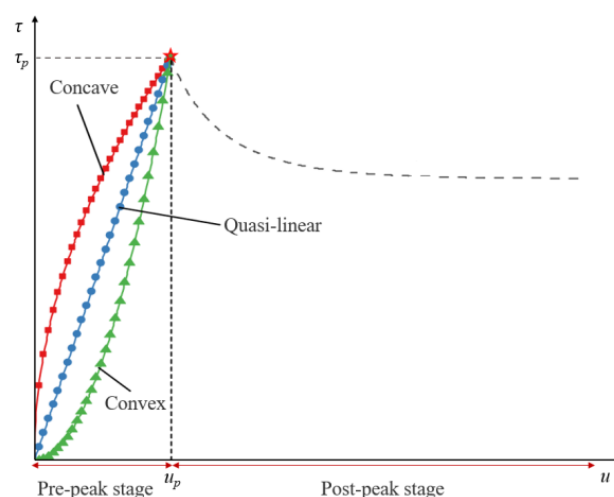


**Figure 2.** Examples of the pre-peak shear stress-shear displacement curve (modified after [51]).

To remedy this limitation, the semi-analytical model based on the Haldane distribution and exponential correction coefficient was built in this paper, which can represent the shear deformation of three kinds of pre-peak curves. Then the shear test data of different types of rock joints were selected for validity verification. Comprehensive comparisons between the proposed model and other existing models were launched to illustrate the superiority of this model.

## 2. Model Development

The statistical damage-based approach is widely used to deal with the constitutive response to study the deformation process and failure mechanism of rock materials [52,53]. According to the statistical damage theory, it is assumed that the damage variable obeys a certain distribution function, such as Weibull distribution [54], improved Harris distribution [55], normal (Gaussian) distribution [56], Haldane distribution [57], etc. A comprehensive review of these distribution functions and corresponding constitutive models is provided by Lin et al. [58]. These distribution functions are widely used in many fields, including geophysics, biology, population growth, and economics [59].

The Weibull distribution function is the most commonly used distribution function to numerically model the rock damage, the expression of which  $F(x)$  is shown in Equation (1) [60,61].

$$F(x) = 1 - e^{-\left(\frac{x}{x_0}\right)^m} \quad (1)$$

where  $x$  is a variable parameter,  $e$  is Euler's number,  $x_0$  and  $m$  are Weibull distribution parameters without clear physical meanings and mathematical definitions [62].

Although previous studies have proved that the results obtained by the Weibull distribution are statistically acceptable, only focusing on some statistical indicators such as coefficient of determination ( $R^2$ ) and root mean square error (RMSE) (see Equation (A1) in Appendix A) may mask the shortcomings of this distribution, and blind use of this method may cause large errors [63]. Beyond that, it has also been documented [64–67] that there

is not enough evidence showing that the Weibull distribution always takes precedence over other distributions and whether the Weibull distribution is the most appropriate statistical distribution function for quasi-brittle materials (such as rock, ceramics, and concrete) is questionable. As Weibull emphasized in his pioneering paper [54], the Weibull distribution is an empirical distribution function, similar to other distribution functions. The establishment of a constitutive model using the Weibull distribution is also a complicated process in which three unknown variables need to be solved according to at least three sets of data [57]. It can be found that the Weibull function for possible prediction of the stress–strain ( $\sigma$ – $\epsilon$ ) relationship may have three unknown constants ( $\lambda$ ,  $m$  and  $\epsilon_0$ ):

$$\sigma = \lambda \left[ 1 - \frac{1}{e^{(\frac{\epsilon}{\epsilon_0})^m}} \right] \quad (2)$$

It is best to use distribution functions with fewer parameters in modeling. Referring to Palchik [68], the Haldane distribution was used to establish the constitutive model of rock joints. As shown in Equation (3), the Haldane distribution contains only two known parameters (2 and 1/2):

$$F(x) = \frac{1}{2} (1 - e^{-2x}) \quad (3)$$

It can be deduced that  $F(x) = 0$  when  $x = 0$ , which is consistent with the fact that the shear stress/shear displacement curve initiates from the origin. Additionally, the graph of Equation (3) is in the first quadrant since the shear displacement is nonnegative, which makes the physical significance of Equation (3) more explicit. Therefore, Equation (3) can be applied to establish a joint shear constitutive curve, namely,

$$\tau = \frac{\alpha}{2} (1 - e^{-2u}) \quad (4)$$

Since the pre-peak curve must pass the peak point ( $u_p, \tau_p$ ), substitute  $u_p$  and  $\tau_p$  into Equation (4) to obtain the expression of  $\alpha$ :

$$\alpha = \frac{2\tau_p}{1 - e^{-2u_p}} \quad (5)$$

Substitute Equation (5) into Equation (4):

$$\tau = \tau_p \left( \frac{1 - e^{-2u}}{1 - e^{-2u_p}} \right) \quad (6)$$

To obtain a model with wider applicability, the correction coefficient  $\left( \frac{1 - e^{-2u}}{1 - e^{-2u_p}} \right)^{\gamma-1}$  is adapted to construct an improved model suitable for describing different pre-peak curves:

$$\tau = \tau_p \left( \frac{1 - e^{-2u}}{1 - e^{-2u_p}} \right) \left( \frac{1 - e^{-2u}}{1 - e^{-2u_p}} \right)^{\gamma-1} = \tau_p \left( \frac{1 - e^{-2u}}{1 - e^{-2u_p}} \right)^{\gamma} \quad (7)$$

Equation (7) is the semi-analytical model based on the Haldane distribution function, which is used to describe the pre-peak stage of the shear stress/shear displacement curve. The model parameter  $\gamma$  can be determined using the statistical method of successive approximations. Whether Equation (7) can predict the pre-peak shear constitutive relationship requires a further comparison between the observed and predicted shear stress/shear displacement curves, which is discussed in Section 3.

### 3. Model Validation

In the first series of verification tests, the shear test results of artificial joints conducted by Bao et al. [69] were adopted. As shown in Figure 3a, the target joints are taken from the face of the Guanshan tunnel in Gansu Province, China, and the lithology of the rock joints

is diorite. The three-dimensional point cloud of target joints was obtained by scanning the collected samples with a handheld 3D laser scanner, and the resin mold was made. Then, three groups of artificial joint samples with different strengths were made according to the mixing ratio shown in Table 1 (numbered as group a, group b and group c). During the shear test, the normal stresses were set as 0.2 MPa, 0.5 MPa, and 1 MPa, respectively. Jointed samples are numbered X-Y-Z, where X represents group number (a, b, c), Y represents the normal stress, and Z represents the shear direction ( $0^\circ$ ,  $90^\circ$ ,  $180^\circ$ , and  $270^\circ$ ). The anisotropic shear test results of each joint sample under different normal stresses are shown in Figure 3b.

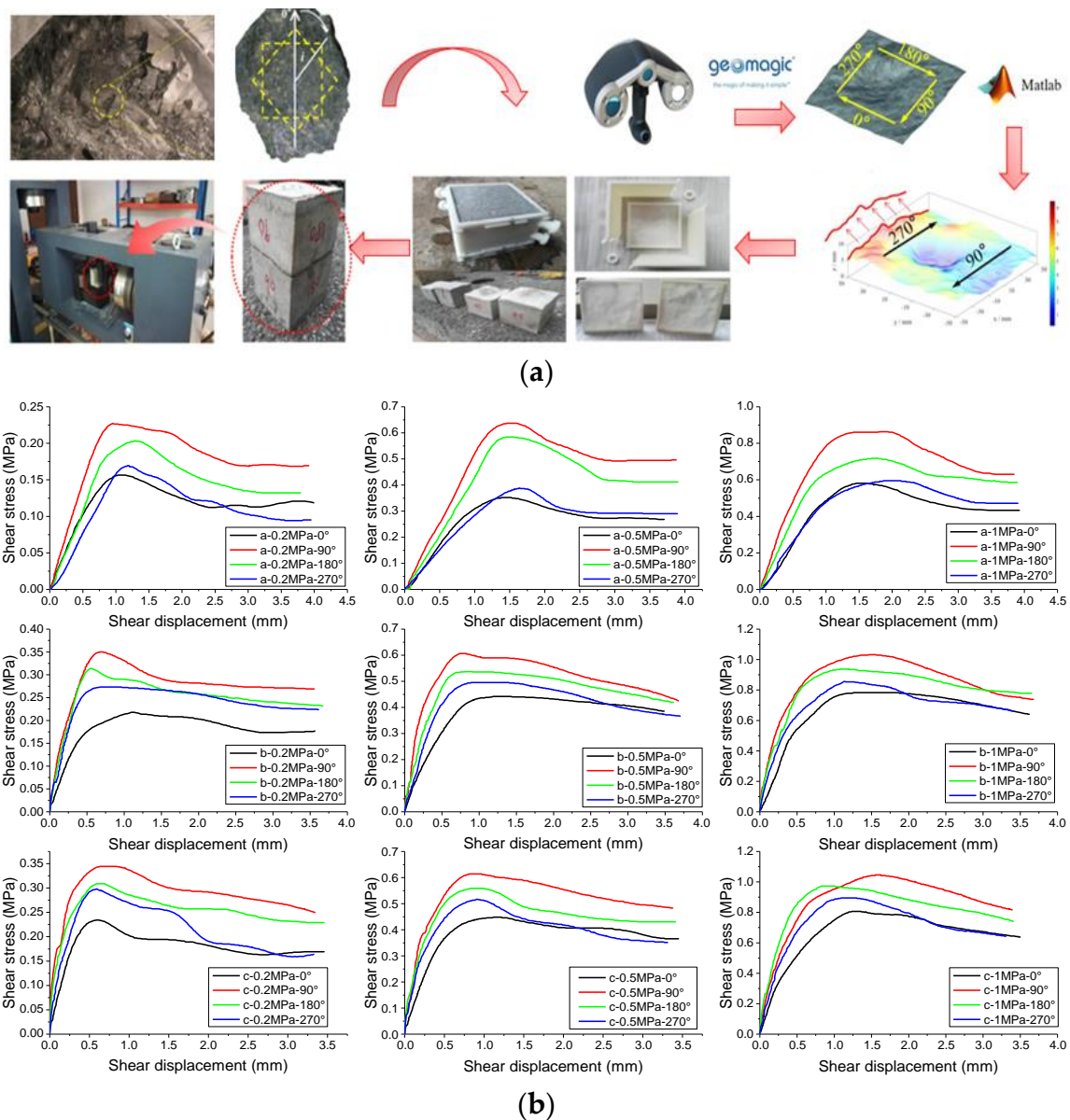


**Figure 3.** Preparation process and shear test results of joint samples, (a) Sample-making process, (b) Shear stress-shear displacement curves [69].

**Table 1.** Ingredient proportions of artificial joints samples [69].

| Group | Water | Cement | Sand | Silicon | Water Reducer |
|-------|-------|--------|------|---------|---------------|
| a     | 1     | 2      | 2    | 0       | 0             |
| b     | 1     | 2      | 3    | 0.1     | 0.1           |
| c     | 1     | 2      | 3    | 0.2     | 0.2           |



To facilitate a comparison of model results, the proposed model was compared with Ban et al. [49] model, Bandis et al. [46] model, and Nassir et al. [48] model. The expressions of each model are as follows:

Ban et al. [49] model:

$$\tau = k_i \left[ \left( 1 - \frac{a}{b} \right) u + \frac{au_p}{b^2} \ln \left( \frac{b^2 u + bu_p}{bu_p} \right) \right] \quad (8)$$

where parameters  $a$  and  $b$  are model parameters, and  $k_i$  is the initial shear stiffness. All three parameters can be obtained by fitting test data.

Bandis et al. [46] model:

$$\tau = \frac{u}{m + nu} \quad (9)$$

where  $m$  represents the reciprocal of the initial shear stiffness and  $n$  is the reciprocal of the horizontal asymptote to the hyperbolic curve. Both  $m$  and  $n$  are positive.

Nassir et al. [48] model:

$$\tau = \frac{k_i u}{1 + \delta u} \quad (10)$$

where parameters  $\delta$  can be obtained by Equation (11):

$$\delta = \frac{1 - \frac{\sigma_n \tan(\varphi_b)}{\tau_p \eta}}{u_p \left( \frac{\sigma_n \tan(\varphi_b)}{\tau_p} - 1 \right)} \quad (11)$$

where  $\eta$  and  $\varphi_b$  are dilation initiation coefficient (ranging from 0 to 1) and basic friction angle, respectively.

According to Refs [70,71], to calibrate the above four models, the expressions of each constitutive model were implemented in Origin software so that we may utilize the Levenberg–Marquardt (L-M) algorithm. The error of each model between the measured stress and the theoretical value is measured by  $R^2$ . As shown in Figure 4, the above four models are successively substituted into the experimental results in Figure 3a to solve. Owing to the limited paper length, only the comparison results of experiment b-0.5MPa-0° are given. The  $R^2$  of each theoretical curve fitted by the proposed model and other models was listed in Table 2, which indicates that the theoretical curves agree well with the experimental results. However, it should be noted that the proposed model only contains one unknown parameter  $\gamma$ , while other models contain multiple unknown parameters. Fewer parameters are the advantage of the proposed model.

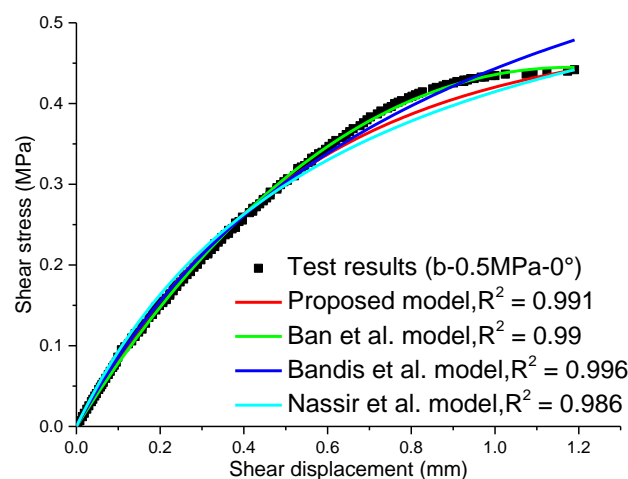


**Figure 4.** Comparison between model and experimental results of b-0.5MPa-0° [46,48,49].

**Table 2.** Fitting effect of model and experimental results.

| Joint Samples | Model Expression of the Proposed Model   | Proposed Model | Ban et al. [49] Model | $R^2$<br>Bandis et al. [46] Model | Nassir et al. [48] Model |
|---------------|--|----------------|-----------------------|-----------------------------------|--------------------------|
| a-0.2MPa-0°   | $\tau = 0.1564 \left( \frac{1 - e^{-2u}}{1 - e^{-2 \times 1.03361}} \right)^{1.28}$  | 0.999          | 0.991                 | 0.997                             | 0.994                    |
| a-0.2MPa-90°  | $\tau = 0.2271 \left( \frac{1 - e^{-2u}}{1 - e^{-2 \times 0.9496}} \right)^{1.425}$  | 0.998          | 0.99                  | 0.98                              | 0.98                     |
| a-0.2MPa-180° | $\tau = 0.2036 \left( \frac{1 - e^{-2u}}{1 - e^{-2 \times 1.2914}} \right)^{1.559}$  | 0.983          | 0.982                 | 0.98                              | 0.98                     |
| a-0.2MPa-270° | $\tau = 0.1693 \left( \frac{1 - e^{-2u}}{1 - e^{-2 \times 1.174}} \right)^{2.184}$   | 0.996          | /                     | 0.97                              | 0.97                     |
| a-0.5MPa-0°   | $\tau = 0.352 \left( \frac{1 - e^{-2u}}{1 - e^{-2 \times 1.388}} \right)^{1.792}$    | 0.999          | 0.994                 | 0.987                             | 0.98                     |
| a-0.5MPa-90°  | $\tau = 0.6369 \left( \frac{1 - e^{-2u}}{1 - e^{-2 \times 1.462}} \right)^{2.208}$   | 0.982          | 0.98                  | 0.981                             | 0.972                    |
| a-0.5MPa-180° | $\tau = 0.584 \left( \frac{1 - e^{-2u}}{1 - e^{-2 \times 1.4486}} \right)^{2.809}$   | 0.977          | /                     | 0.96                              | 0.97                     |
| a-0.5MPa-270° | $\tau = 0.3887 \left( \frac{1 - e^{-2u}}{1 - e^{-2 \times 1.6379}} \right)^{2.355}$  | 0.983          | 0.991                 | 0.983                             | 0.983                    |
| a-1.0MPa-0°   | $\tau = 0.5807 \left( \frac{1 - e^{-2u}}{1 - e^{-2 \times 1.462}} \right)^{2.0407}$  | 0.999          | 0.99                  | 0.983                             | 0.974                    |
| a-1.0MPa-90°  | $\tau = 0.8603 \left( \frac{1 - e^{-2u}}{1 - e^{-2 \times 1.421}} \right)^{1.3905}$  | 0.998          | 0.992                 | 0.98                              | 0.984                    |
| a-1.0MPa-180° | $\tau = 0.7179 \left( \frac{1 - e^{-2u}}{1 - e^{-2 \times 1.6919}} \right)^{1.427}$  | 0.995          | 0.993                 | 0.985                             | 0.993                    |
| a-1.0MPa-270° | $\tau = 0.5947 \left( \frac{1 - e^{-2u}}{1 - e^{-2 \times 1.8727}} \right)^{1.846}$  | 0.996          | 0.995                 | 0.986                             | 0.99                     |
| b-0.2MPa-0°   | $\tau = 0.2146 \left( \frac{1 - e^{-2u}}{1 - e^{-2 \times 1.0227}} \right)^{0.808}$  | 0.985          | 0.99                  | 0.981                             | 0.983                    |
| b-0.2MPa-90°  | $\tau = 0.35 \left( \frac{1 - e^{-2u}}{1 - e^{-2 \times 0.668}} \right)^{0.82}$      | 0.994          | 0.989                 | 0.984                             | 0.985                    |
| b-0.2MPa-180° | $\tau = 0.3142 \left( \frac{1 - e^{-2u}}{1 - e^{-2 \times 0.5537}} \right)^{0.921}$  | 0.998          | 0.998                 | 0.988                             | 0.98                     |
| b-0.2MPa-270° | $\tau = 0.2731 \left( \frac{1 - e^{-2u}}{1 - e^{-2 \times 0.6777}} \right)^{0.7503}$ | 0.945          | 0.993                 | 0.975                             | 0.973                    |
| b-0.5MPa-0°   | $\tau = 0.4419 \left( \frac{1 - e^{-2u}}{1 - e^{-2 \times 1.1901}} \right)^{1.0361}$ | 0.991          | 0.99                  | 0.996                             | 0.986                    |
| b-0.5MPa-90°  | $\tau = 0.6062 \left( \frac{1 - e^{-2u}}{1 - e^{-2 \times 0.7438}} \right)^{0.72}$   | 0.979          | 0.99                  | 0.989                             | 0.988                    |
| b-0.5MPa-180° | $\tau = 0.5371 \left( \frac{1 - e^{-2u}}{1 - e^{-2 \times 0.8265}} \right)^{0.80}$   | 0.983          | 0.979                 | 0.994                             | 0.984                    |
| b-0.5MPa-270° | $\tau = 0.4952 \left( \frac{1 - e^{-2u}}{1 - e^{-2 \times 0.8926}} \right)^{0.906}$  | 0.987          | 0.99                  | 0.991                             | 0.984                    |
| b-1.0MPa-0°   | $\tau = 0.782 \left( \frac{1 - e^{-2u}}{1 - e^{-2 \times 1.2619}} \right)^{1.118}$   | 0.992          | 0.99                  | 0.992                             | 0.99                     |
| b-1.0MPa-90°  | $\tau = 1.0315 \left( \frac{1 - e^{-2u}}{1 - e^{-2 \times 1.4763}} \right)^{0.711}$  | 0.996          | 0.99                  | 0.99                              | 0.987                    |
| b-1.0MPa-180° | $\tau = 0.9371 \left( \frac{1 - e^{-2u}}{1 - e^{-2 \times 1.0909}} \right)^{0.764}$  | 0.976          | 0.992                 | 0.981                             | 0.979                    |
| b-1.0MPa-270° | $\tau = 0.8562 \left( \frac{1 - e^{-2u}}{1 - e^{-2 \times 1.1405}} \right)^{0.862}$  | 0.997          | 0.99                  | 0.991                             | 0.99                     |
| c-0.2MPa-0°   | $\tau = 0.2341 \left( \frac{1 - e^{-2u}}{1 - e^{-2 \times 0.5905}} \right)^{0.759}$  | 0.976          | 0.998                 | 0.976                             | 0.998                    |
| c-0.2MPa-90°  | $\tau = 0.344 \left( \frac{1 - e^{-2u}}{1 - e^{-2 \times 0.6338}} \right)^{0.467}$   | 0.935          | 0.96                  | 0.951                             | 0.94                     |
| c-0.2MPa-180° | $\tau = 0.3086 \left( \frac{1 - e^{-2u}}{1 - e^{-2 \times 0.5918}} \right)^{0.523}$  | 0.98           | 0.996                 | 0.97                              | 0.96                     |
| c-0.2MPa-270° | $\tau = 0.2981 \left( \frac{1 - e^{-2u}}{1 - e^{-2 \times 0.5917}} \right)^{0.683}$  | 0.985          | 0.995                 | 0.98                              | 0.982                    |
| c-0.5MPa-0°   | $\tau = 0.4476 \left( \frac{1 - e^{-2u}}{1 - e^{-2 \times 1.128}} \right)^{0.803}$   | 0.975          | 0.99                  | 0.971                             | 0.973                    |

Table 2. Cont.

| Joint Samples | Model Expression of the Proposed Model   | Proposed Model | Ban et al. [49] Model | $R^2$<br>Bandis et al. [46] Model | Nassir et al. [48] Model |
|---------------|--|----------------|-----------------------|-----------------------------------|--------------------------|
| c-0.5MPa-90°  | $\tau = 0.6132 \left( \frac{1 - e^{-2u}}{1 - e^{-2 \times 0.8099}} \right)^{0.6673}$ | 0.988          | 0.99                  | 0.964                             | 0.983                    |
| c-0.5MPa-180° | $\tau = 0.558 \left( \frac{1 - e^{-2u}}{1 - e^{-2 \times 0.8316}} \right)^{0.622}$   | 0.983          | 0.985                 | 0.979                             | 0.976                    |
| c-0.5MPa-270° | $\tau = 0.517 \left( \frac{1 - e^{-2u}}{1 - e^{-2 \times 0.911}} \right)^{0.661}$    | 0.99           | 0.99                  | 0.981                             | 0.98                     |
| c-1.0MPa-0°   | $\tau = 0.806 \left( \frac{1 - e^{-2u}}{1 - e^{-2 \times 1.239}} \right)^{1.099}$    | 0.995          | 0.99                  | 0.982                             | 0.981                    |
| c-1.0MPa-90°  | $\tau = 1.0449 \left( \frac{1 - e^{-2u}}{1 - e^{-2 \times 1.5556}} \right)^{0.828}$  | 0.997          | 0.99                  | 0.977                             | 0.983                    |
| c-1.0MPa-180° | $\tau = 0.9714 \left( \frac{1 - e^{-2u}}{1 - e^{-2 \times 0.8282}} \right)^{0.7175}$ | 0.984          | 0.996                 | 0.973                             | 0.981                    |
| c-1.0MPa-270° | $\tau = 0.8942 \left( \frac{1 - e^{-2u}}{1 - e^{-2 \times 1.0947}} \right)^{0.8825}$ | 0.998          | 0.99                  | 0.981                             | 0.983                    |

Interestingly, in the process of solving, it was found that Ban et al. [49] model, Bandis et al. [46] model, and Nassir et al. [48] model performed poorly for some test results at the initial loading stage, i.e., the prediction results were significantly higher than the test results. On the contrary, the proposed model performed well in the entire loading stage. Taking the test results of a-0.5MPa-0° and a-1MPa-0° as an example, the application of the above four models is presented in Figure 5. It can be found that the Ban et al. [49] model, Bandis et al. [46] model, and Nassir et al. [48] model cannot describe the nonlinear deformation characteristics at the initial loading stage. To facilitate understanding, the shear stress/shear displacement curves of the initial loading stage are excerpted and magnified (i.e., the enlarged view in Figure 5). The  $R^2$  of the above four models in the enlarged view is shown in Figure 6. It can be seen that the fitting effect of the proposed model is still good ( $R^2 > 0.9$ ), while the fitting effect of the other three models is relatively poor (0.539–0.834). In addition, the proposed model guarantees that the model curve passes the peak point, whereas the Ban et al. [49] model and Bandis et al. [46] model do not. All these demonstrate the superiority of the proposed model.

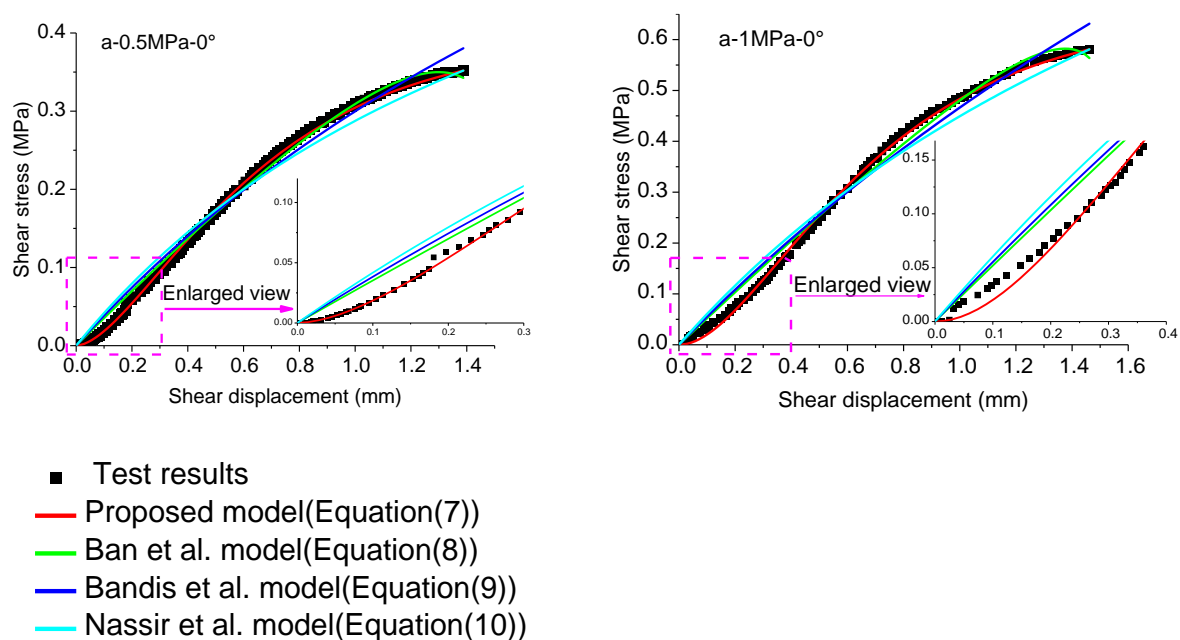


Figure 5. The comparison between each model and experimental results [46,48,49].



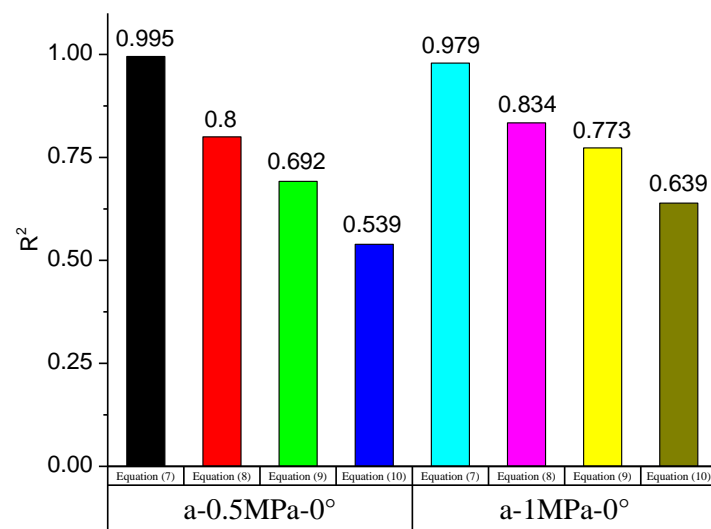


Figure 6.  $R^2$  of each model.

#### 4. Discussion

The shape of the pre-peak shear curve of rock joints depends on roughness, mechanical properties, geological environment, and other perturbation factors. Subjected to certain environmental factors, such as freeze–thaw and immersion, the pre-peak constitutive curve of rock joints is reflected in a convex-type curve. During the initial loading stage, the hangingwall and footwall of rock joints are compressed, and the internal pores and cracks are compacted. This results in a downward concave shear stress/shear displacement curve, and the tangent slope of the curve increases as the shear displacement is applied [72]. There would be a significant error induced by the use of Equations (8)–(10) when describing the pre-peak mechanical behavior of such joints.

The typical convex-type test results in Refs. [73,74] are selected for verification, as shown in Figure 7a,b, which can still be well characterized by the proposed model. However, applying hyperbolic models such as the Ban et al. [49] model, Bandis et al. [46] model, and Nassir et al. [48] model to this validation will result in the parameter fitting being negative (contradictory with each model parameter being greater than 0) or not converging (Figure 8). This is due to the functional nature of the hyperbolic model itself. Under limited conditions (such as model parameters greater than 0), they cannot effectively describe the convex-type curve.

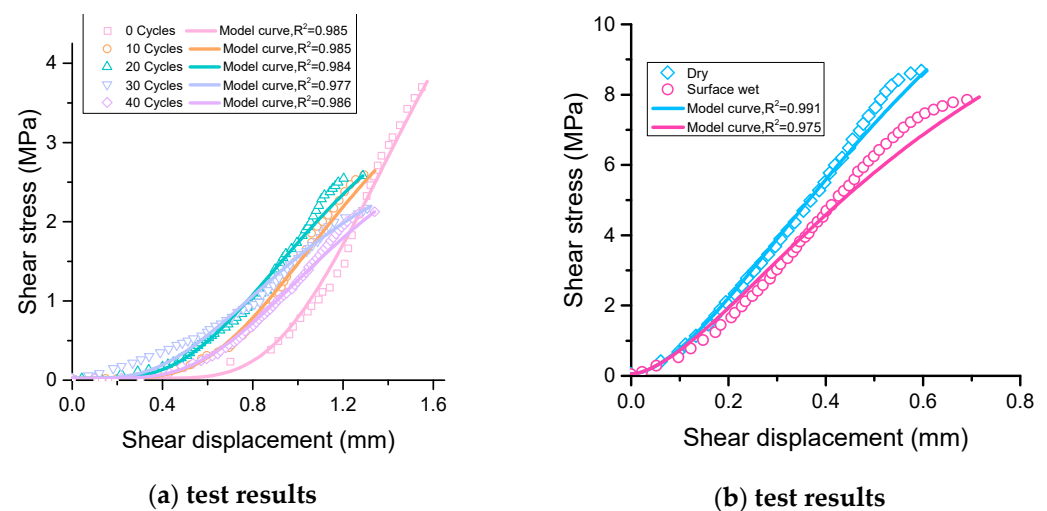
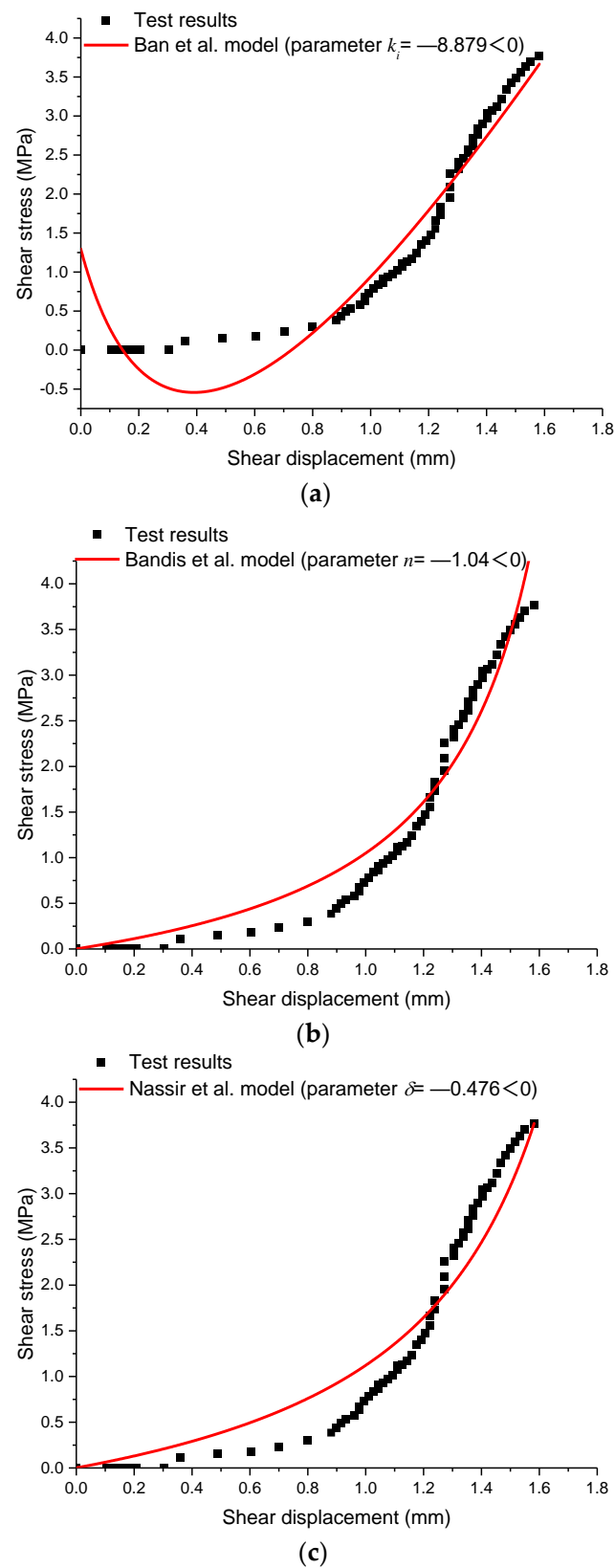


Figure 7. Comparison of test results [73,74] with model curves.



**Figure 8.** Comparison of test results (0 cycle) [73] with existing models, (a) Ban et al. [49] model, (b) Bandis et al. [46] model, (c) Nassir et al. [48] model.

The experiment is one of the most fundamental and effective research methods. In Section 3, this paper only focuses on the performance of the proposed model in describing

the shear deformation of rock joints in laboratory experiments. Considering that there are many limitations of laboratory experiments, such as difficult field sampling, disturbance to the original state of samples, and defects in laboratory test instruments, the results may not be consistent with reality [75]. Therefore, the in situ shear test, which can obtain the mechanical parameters consistent with engineering practice, was employed.

Taking the test results [76,77] under in-situ conditions as an example, the performance of the model in reproducing in situ rock joint behavior is studied. Figure 9 shows the comparison of shear test data with limestone joints collected from the Lanjiberna limestone mine (located in Odisha, India) with model curves. Figure 10 shows the comparison of shear test results and model curves for sandstone joint samples collected from the upper reservoir of the Azad pump storage power plant project in western Iran. The corresponding fitting curves from the proposed model are well matched with the experimental data in Figures 9 and 10. Obviously, from Figures 9 and 10 (all  $R^2$  values are greater than 0.94), it is not difficult to find that the proposed model can also represent the pre-peak shear deformation behavior of in-situ rock joints to a certain extent. Of course, it is still a complex task to estimate the shear behavior of rock joints under in situ conditions due to various influencing factors presented in the field. We will study the performance of this model in reproducing in situ rock joint behavior in geotechnical engineering features such as rock slopes and tunnels in the future.

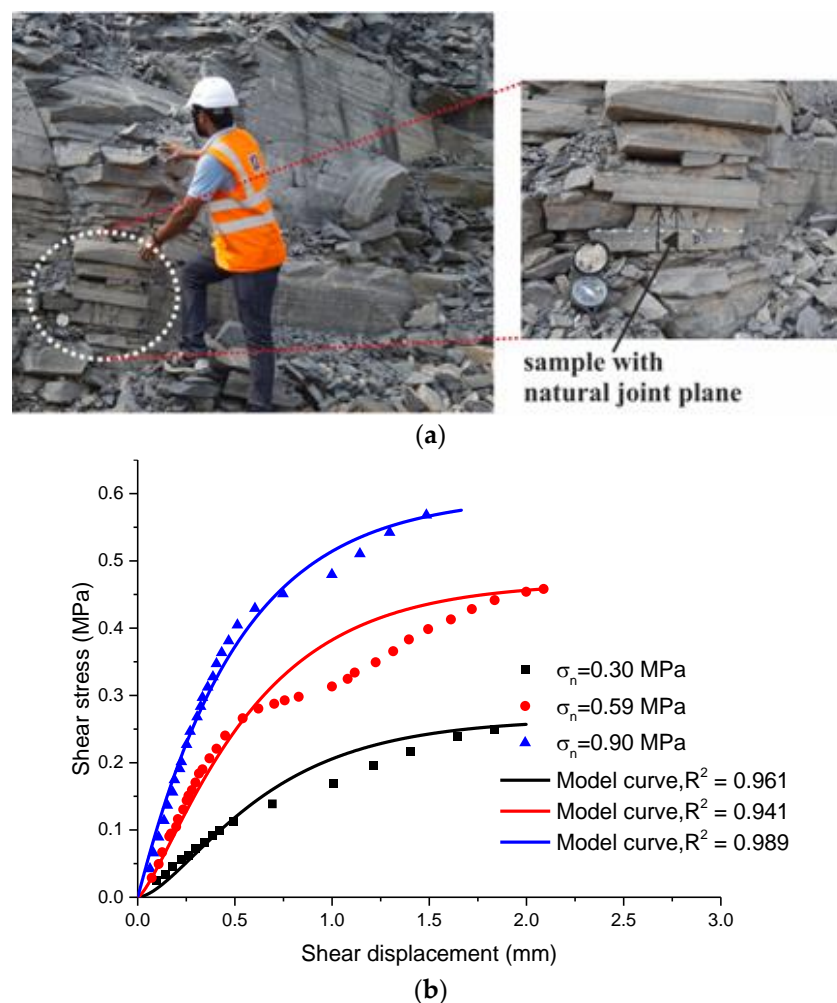


**Figure 9.** Comparison of in situ test results [76] with model curves, (a) sample collection, (b) shear stress-shear displacement curve.

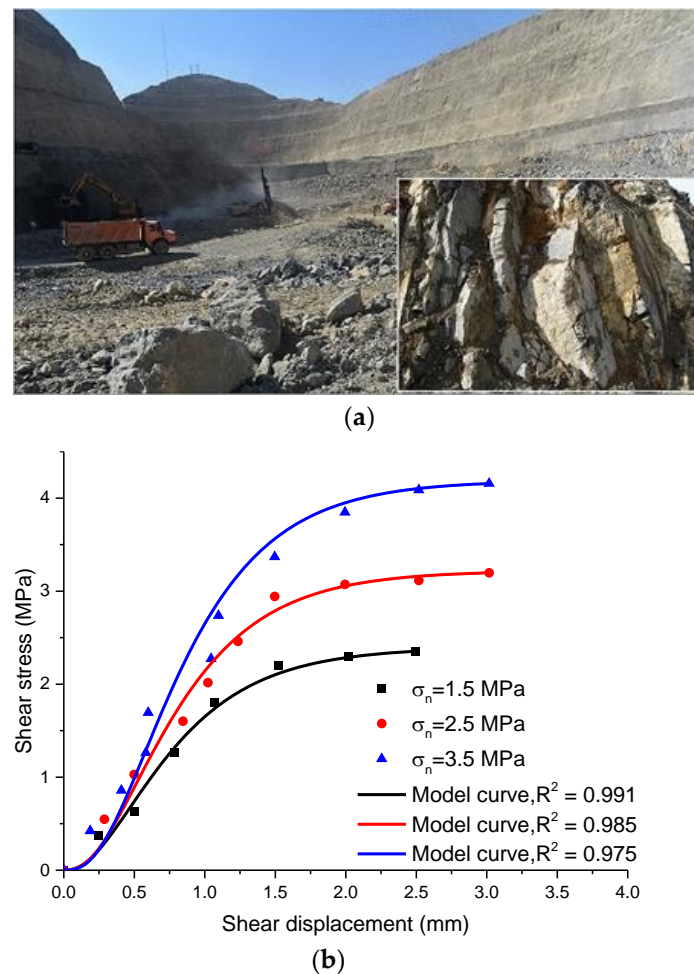


**Figure 10.** Comparison of in situ test results [77] with model curves, (a) sample collection, (b) shear stress-shear displacement curve.

## 5. Conclusions

Based on Haldane distribution, a new semi-analytical model for the pre-peak shear deformation of rock joints is established. The effectiveness of the model was verified by laboratory and in situ experimental data. To better demonstrate the advantages of this model, it is compared with existing models. The results show that the results of the proposed model are similar to those of the existing models for quasilinear-type and concave-type curves. For convex-type curves, the effect of the proposed model is much better than that of the existing models. In addition, compared with existing models that have at least two or more parameters to be fitted, the model in this paper contains only one parameter, which is convenient for application.

**Author Contributions:** Conceptualization, S.X. and Y.C.; data curation, S.X.; funding acquisition, H.L. and Z.H.; investigation, H.L. and Z.H.; methodology, S.X. and H.D.; writing—original draft, S.X. and Y.C.; writing—review and editing, Z.H. and D.L. All authors have read and agreed to the published version of the manuscript.

**Funding:** This paper received financial funding from the National Natural Science Foundation of China (No. 52104111 and 42277175) and Postgraduate Research and Practice Innovation Program of Jiangsu Province (No. KYCX21\_0119).

**Data Availability Statement:** Data available on request due to privacy restrictions.

**Conflicts of Interest:** The authors declare no conflict of interest.

## Appendix A

The coefficient of determination ( $R^2$ ) and root mean square error (RMSE) can be used to assess the matching effect of the proposed model against the experimental data, which can be calculated by Equation (A1).

$$\begin{cases} R^2 = 1 - \frac{N-1}{N-2} \times \frac{\sum_{i=1}^N (y_{test}^i - y_{cal}^i)^2}{\sum_{i=1}^N (y_{test}^i - y_{ave})^2} \\ RMSE = \sqrt{\frac{\sum_{i=1}^N (y_{test}^i - y_{cal}^i)^2}{N}} \end{cases} \quad (A1)$$

where  $N$  is the number of measured points;  $y_{test}$  and  $y_{cal}$  are, respectively, the measured stress and the theoretical stress; and  $y_{ave}$  is the average of the  $y_{test}$ .

## References

- Schreyer, H.; Sulsky, D. Constitutive and numerical framework for modeling joints and faults in rock. *Int. J. Numer. Anal. Met.* **2016**, *40*, 1253–1283. [\[CrossRef\]](#)
- Luo, X.; Cao, P.; Liu, T.; Zhao, Q.; Meng, G.; Fan, Z.; Xie, W. Mechanical behaviour of anchored rock containing weak interlayer under uniaxial compression: Laboratory test and coupled dem-fem simulation. *Minerals* **2022**, *12*, 492. [\[CrossRef\]](#)
- Yong, R.; Qin, J.-B.; Huang, M.; Du, S.-G.; Liu, J.; Hu, G.-J. An innovative sampling method for determining the scale effect of rock joints. *Rock Mech. Rock Eng.* **2019**, *52*, 935–946. [\[CrossRef\]](#)
- Hu, G.J.; Ma, G.; Liu, J.; Qi, K. Size effect of the number of parallel joints on uniaxial compressive strength and characteristic strength. *Minerals* **2022**, *12*, 62. [\[CrossRef\]](#)
- Lin, Q.; Cao, P.; Meng, J.; Cao, R.; Zhao, Z. Strength and failure characteristics of jointed rock mass with double circular holes under uniaxial compression: Insights from discrete element method modelling. *Theor. Appl. Fract. Mec.* **2020**, *109*, 102692. [\[CrossRef\]](#)
- Fan, X.; Yu, H.; Deng, Z.; He, Z.; Zhao, Y. Cracking and deformation of cuboidal sandstone with a single nonpenetrating flaw under uniaxial compression. *Theor. Appl. Fract. Mec.* **2022**, *119*, 103284. [\[CrossRef\]](#)
- Saadat, M.; Taheri, A. A cohesive discrete element based approach to characterizing the shear behavior of cohesive soil and clay-infilled rock joints. *Comput. Geotech.* **2019**, *114*, 103109. [\[CrossRef\]](#)
- Xie, S.; Han, Z.; Hu, H.; Lin, H. Application of a novel constitutive model to evaluate the shear deformation of discontinuity. *Eng. Geol.* **2022**, *304*, 106693. [\[CrossRef\]](#)
- Cai, W.; Zhu, H.; Liang, W. Three-dimensional stress rotation and control mechanism of deep tunneling incorporating generalized Zhang–Zhu strength-based forward analysis. *Eng. Geol.* **2022**, *308*, 106806. [\[CrossRef\]](#)
- Yang, Z.; Wu, Y.; Zhou, Y.; Tang, H.; Fu, S. Assessment of machine learning models for the prediction of rate-dependent compressive strength of rocks. *Minerals* **2022**, *12*, 731. [\[CrossRef\]](#)
- Petrounias, P.; Giannakopoulou, P.P.; Rogkala, A.; Lampropoulou, P.; Koutsopoulou, E.; Papoulis, D.; Tsikouras, B.; Hatzipanagiotou, K. The impact of secondary phyllosilicate minerals on the engineering properties of various igneous aggregates from greece. *Minerals* **2018**, *8*, 329. [\[CrossRef\]](#)
- Gronen, L.H.; Sindern, S.; Katzmarzyk, J.L.; Bormann, U.; Hellmann, A.; Wotruba, H.; Meyer, F.M. Mineralogical and chemical characterization of zr-ree-nb ores from khalzan buregtei (mongolia) approaches to more efficient extraction of rare metals from alkaline granitoids. *Minerals* **2019**, *9*, 217. [\[CrossRef\]](#)
- Wang, J.A.; Park, H.D. Fluid permeability of sedimentary rocks in a complete stress-strain process. *Eng. Geol.* **2002**, *63*, 291–300. [\[CrossRef\]](#)
- Xie, S.; Lin, H.; Cheng, C.; Chen, Y.; Wang, Y.; Zhao, Y.; Yong, W. Shear strength model of joints based on Gaussian smoothing method and macro-micro roughness. *Comput. Geotech.* **2022**, *143*, 104605. [\[CrossRef\]](#)
- Patel, S.; Martin, C.D. Effect of stress path on the failure envelope of intact crystalline rock at low confining stress. *Minerals* **2020**, *10*, 1119. [\[CrossRef\]](#)
- Xu, X.Q.; Wu, W.L.; Xu, W.B. Sulfate-dependent shear behavior of cementing fiber-reinforced tailings and rock. *Minerals* **2020**, *10*, 1032. [\[CrossRef\]](#)
- Han, Z.; Li, D.; Li, X. Dynamic mechanical properties and wave propagation of composite rock-mortar specimens based on SHPB tests. *Int. J. Min. Sci. Technol.* **2022**, *32*, 793–806. [\[CrossRef\]](#)
- Wu, Y.; Zhou, Y. Hybrid machine learning model and Shapley additive explanations for compressive strength of sustainable concrete. *Constr. Build. Mater.* **2022**, *330*, 127298. [\[CrossRef\]](#)
- Han, Z.; Li, D.; Li, X. Effects of axial pre-force and loading rate on Mode I fracture behavior of granite. *Int. J. Rock Mech. Min. Sci.* **2022**, *157*, 105172. [\[CrossRef\]](#)

20. Pardoën, B.; Seyed, D.M.; Collin, F. Shear banding modelling in cross-anisotropic rocks. *Int. J. Solids Struct.* **2015**, *72*, 63–87. [\[CrossRef\]](#)
21. Bahaaddini, M.; Hagan, P.C.; Mitra, R.; Hebblewhite, B.K. Scale effect on the shear behaviour of rock joints based on a numerical study. *Eng. Geol.* **2014**, *181*, 212–223. [\[CrossRef\]](#)
22. Asadollahi, P.; Tonon, F. Constitutive model for rock fractures: Revisiting Barton’s empirical model. *Eng. Geol.* **2010**, *113*, 11–32. [\[CrossRef\]](#)
23. Mehrishal, S.; Sharifzadeh, M.; Song, J.J.; Shahriar, K. An investigation of the possibility of estimating the residual shear strength of rough joints using planar small joint in limestone rocks. *J. Struct. Geol.* **2021**, *142*, 104220. [\[CrossRef\]](#)
24. Wang, X.Q.; Kang, H.P.; Gao, F.Q. Numerical investigation on the shear behavior of jointed coal mass. *Comput. Geotech.* **2019**, *106*, 274–285. [\[CrossRef\]](#)
25. Karami, A.; Stead, D. Asperity degradation and damage in the direct shear test: A hybrid fem/dem approach. *Rock Mech. Rock Eng.* **2008**, *41*, 229–266. [\[CrossRef\]](#)
26. Asadi, M.S.; Rasouli, V.; Barla, G. A laboratory shear cell used for simulation of shear strength and asperity degradation of rough rock fractures. *Rock Mech. Rock Eng.* **2013**, *46*, 683–699. [\[CrossRef\]](#)
27. Bahaaddini, M.; Hagan, P.C.; Mitra, R.; Khosravi, M.H. Experimental and numerical study of asperity degradation in the direct shear test. *Eng. Geol.* **2016**, *204*, 41–52. [\[CrossRef\]](#)
28. Cai, W.; Zhu, H.; Liang, W. Three-dimensional tunnel face extrusion and reinforcement effects of underground excavations in deep rock masses. *Int. J. Rock Mech. Min. Sci.* **2022**, *150*, 104999. [\[CrossRef\]](#)
29. Meng, F.; Zhou, H.; Li, S.; Zhang, C.; Wang, Z.; Kong, L.; Zhang, L. Shear behaviour and acoustic emission characteristics of different joints under various stress levels. *Rock Mech. Rock Eng.* **2016**, *49*, 4919–4928. [\[CrossRef\]](#)
30. Cui, G.; Zhang, C.; Han, H.; Zeng, Z.; Zhou, H.; Jingjing, L.U. Experiment study on shear behavior of artificial joint under CNL and CNS boundary conditions. *Chin. J. Rock Mech. Eng.* **2019**, *38*, 3384–3392.
31. Fan, W.; Cao, P.; Long, L. Degradation of joint surface morphology, shear behavior and closure characteristics during cyclic loading. *J. Cent South Univ.* **2018**, *25*, 653–661. [\[CrossRef\]](#)
32. Jing, L. A review of techniques, advances and outstanding issues in numerical modelling for rock mechanics and rock engineering. *Int. J. Rock Mech. Min. Sci.* **2003**, *40*, 283–353. [\[CrossRef\]](#)
33. Muralha, J.; Grasselli, G.; Tatone, B.; Blumel, M.; Chryssanthakis, P.; Jiang, Y.J. ISRM Suggested Method for Laboratory Determination of the Shear Strength of Rock Joints: Revised Version. *Rock Mech. Rock Eng.* **2014**, *47*, 291–302. [\[CrossRef\]](#)
34. Xie, S.J.; Lin, H.; Chen, Y.F.; Yong, R.; Xiong, W.; Du, S.G. A damage constitutive model for shear behavior of joints based on determination of the yield point. *Int. J. Rock Mech. Min. Sci.* **2020**, *128*, 104269. [\[CrossRef\]](#)
35. Vakili, A. An improved unified constitutive model for rock material and guidelines for its application in numerical modelling. *Comput. Geotech.* **2016**, *80*, 261–282. [\[CrossRef\]](#)
36. Cai, W.; Zhu, H.; Liang, W.; Wang, X.; Su, C.; Wei, X. A post-peak dilatancy model for soft rock and its application in deep tunnel excavation. *J. Rock Mech. Geotech. Eng.* **2022**. [\[CrossRef\]](#)
37. Cai, W.; Zhu, H.; Liang, W.; Vu, B.; Su, C.; Zhang, K.; Wang, X. Three-dimensional forward analysis and real-time design of deep tunneling based on digital in-situ testing. *Int. J. Mech. Sci.* **2022**, *226*, 107385. [\[CrossRef\]](#)
38. Singh, H.K.; Basu, A. Evaluation of existing criteria in estimating shear strength of natural rock discontinuities. *Eng. Geol.* **2018**, *232*, 171–181. [\[CrossRef\]](#)
39. Develi, K. Computation of direction dependent joint surface parameters through the algorithm of triangular prism surface area method: A theoretical and experimental study. *Int. J. Solids Struct.* **2020**, *202*, 895–911. [\[CrossRef\]](#)
40. Xie, S.J.; Lin, H.; Wang, Y.X.; Chen, Y.F.; Xiong, W.; Zhao, Y.L.; Du, S. A statistical damage constitutive model considering whole joint shear deformation. *Int. J. Damage Mech.* **2020**, *29*, 988–1008. [\[CrossRef\]](#)
41. Xie, S.J.; Han, Z.Y.; Chen, Y.F.; Wang, Y.X.; Zhao, Y.L.; Lin, H. Constitutive modeling of rock materials considering the void compaction characteristics. *Arch. Civ. Mech. Eng.* **2022**, *22*, 60. [\[CrossRef\]](#)
42. Lin, Q.B.; Cao, P.; Wen, G.P.; Meng, J.J.; Cao, R.H.; Zhao, Z.Y. Crack coalescence in rock-like specimens with two dissimilar layers and pre-existing double parallel joints under uniaxial compression. *Int. J. Rock Mech. Min. Sci.* **2021**, *139*, 104621. [\[CrossRef\]](#)
43. Goodman, R.E. *Methods of Geological Engineering in Discontinuous Rocks*; West Publishing, Co.: St. Paul, MN, USA, 1976.
44. Saeb, S.; Amadei, B. Modelling rock joints under shear and normal loading. *Int. J. Rock Mech. Min. Sci.* **1992**, *29*, 267–278. [\[CrossRef\]](#)
45. Kulhawy, F.H. Stress deformation properties of rock and rock discontinuities. *Eng. Geol.* **1975**, *9*, 327–350. [\[CrossRef\]](#)
46. Bandis, S.C.; Lumsden, A.C.; Barton, N.R. Fundamentals of rock joint deformation. *Int. J. Rock Mech. Min. Sci.* **1983**, *20*, 249–268. [\[CrossRef\]](#)
47. Desai, C.S.; Fishman, K.L. Plasticity-based constitutive model with associated testing for joints. *Int. J. Rock Mech. Min. Sci.* **1991**, *28*, 15–26. [\[CrossRef\]](#)
48. Nassir, M.; Settari, A.; Wan, R. Joint stiffness and deformation behaviour of discontinuous rock. *J. Can. Petrol. Technol.* **2010**, *49*, 78–86. [\[CrossRef\]](#)
49. Ban, L.; Qi, C.; Shan, R.; Tao, Z.; Xia, C.; Jiang, K. Pre-peak shear constitutive model considering the softening shear stiffness and its influencing factors. *J. China Coal. Soc.* **2018**, *43*, 2765–2772. (In Chinese)



50. Kou, M.M.; Liu, X.R.; Tang, S.D.; Wang, Y.T. Experimental study of the prepeak cyclic shear mechanical behaviors of artificial rock joints with multiscale asperities. *Soil Dyn. Earthq. Eng.* **2019**, *120*, 58–74. [\[CrossRef\]](#)
51. Shen, H.; Liu, Y.; Liu, B.; Li, H.; Wu, D.; Peng, B. Nonlinear theoretical model for describing shear mechanical behaviors of rock joints. *Chin. J. Rock Mech. Eng.* **2021**, *40*, 2421–2433.
52. Zhao, H.; Zhou, S.; Zhao, M.H.; Shi, C.J. Statistical micromechanics-based modeling for low-porosity rocks under conventional triaxial compression. *Int. J. Geomech.* **2018**, *18*, 04018019. [\[CrossRef\]](#)
53. Li, X.; Cao, W.-G.; Su, Y.-H. A statistical damage constitutive model for softening behavior of rocks. *Eng. Geol.* **2012**, *143*, 1–17. [\[CrossRef\]](#)
54. Weibull, W. A statistical distribution function of wide applicability. *J. Appl. Mech.* **1951**, *18*, 293–297. [\[CrossRef\]](#)
55. Xie, S.J.; Lin, H.; Wang, Y.X.; Cao, R.H.; Yong, R.; Du, S.G.; Li, J. Nonlinear shear constitutive model for peak shear-type joints based on improved Harris damage function. *Arch. Civ. Mech. Eng.* **2020**, *20*, 1–14. [\[CrossRef\]](#)
56. Cao, W.G.; Li, X.; Zhao, H. Damage constitutive model for strain-softening rock based on normal distribution and its parameter determination. *J. Cent. South Univ.* **2007**, *14*, 719–724. [\[CrossRef\]](#)
57. Palchik, V. Stress-strain model for carbonate rocks based on Haldane's distribution function. *Rock Mech. Rock Eng.* **2006**, *39*, 215–232. [\[CrossRef\]](#)
58. Lin, H.; Feng, J.J.; Cao, R.H.; Xie, S.J. Comparative analysis of rock damage models based on different distribution functions. *Geotech. Geol. Eng.* **2021**, *40*, 301–310. [\[CrossRef\]](#)
59. Sun, Z.; Niu, D.; Wang, X.; Zhang, L.; Luo, D. Bond behavior of coral aggregate concrete and corroded Cr alloy steel bar. *J. Build. Eng.* **2022**, *61*, 105294. [\[CrossRef\]](#)
60. Wang, Z.-L.; Li, Y.-C.; Wang, J.G. A damage-softening statistical constitutive model considering rock residual strength. *Comput. Geosci.* **2007**, *33*, 1–9. [\[CrossRef\]](#)
61. Yang, B.C.; Xue, L.; Wang, M.M. Evolution of the shape parameter in the Weibull distribution for brittle rocks under uniaxial compression. *Arab. J. Geosci.* **2018**, *11*, 1–7. [\[CrossRef\]](#)
62. Shen, P.; Tang, H.; Wang, D.; Ning, Y.; Zhang, Y.; Su, X. A statistical damage constitutive model based on unified strength theory for embankment rocks. *Mar. Georesour. Geotec.* **2020**, *38*, 818–829. [\[CrossRef\]](#)
63. Xie, S.J.; Lin, H.; Chen, Y.F.; Wang, Y.X. A new nonlinear empirical strength criterion for rocks under conventional triaxial compression. *J. Cent. South Univ.* **2021**, *28*, 1448–1458. [\[CrossRef\]](#)
64. Deng, J.A.; Gu, D.S. On a statistical damage constitutive model for rock materials. *Comput. Geosci.* **2011**, *37*, 122–128. [\[CrossRef\]](#)
65. Lu, C.S.; Danzer, R.; Fischer, F.D. Fracture statistics of brittle materials: Weibull or normal distribution. *Phys. Rev. E* **2002**, *65*, 067102. [\[CrossRef\]](#) [\[PubMed\]](#)
66. Basu, B.; Tiwari, D.; Kundu, D.; Prasad, R. Is Weibull distribution the most appropriate statistical strength distribution for brittle materials? *Ceram. Int.* **2009**, *35*, 237–246. [\[CrossRef\]](#)
67. Zhou, X.P.; Yang, H.Q. Micromechanical modeling of dynamic compressive responses of mesoscopic heterogeneous brittle rock. *Theor. Appl. Fract. Mec.* **2007**, *48*, 1–20. [\[CrossRef\]](#)
68. Palchik, V. Simple stress–strain model of very strong limestones and dolomites for engineering practice. *Geomech. Geophys. Geo-Energy Geo-Resour.* **2019**, *5*, 345–356. [\[CrossRef\]](#)
69. Bao, H.; Xu, X.; Lan, H.; Yan, C.; Xu, J. Stiffness model of rock joint by considering anisotropic morphology. *J. Traffic Transp. Eng.* **2021**, *11*, 1–18. (In Chinese)
70. Wang, S.; Chester, S.A. Experimental characterization and continuum modeling of inelasticity in filled rubber-like materials. *Int. J. Solids Struct.* **2018**, *136*, 125–136. [\[CrossRef\]](#)
71. Wang, S.; Chester, S.A. Modeling thermal recovery of the Mullins effect. *Mech. Mater.* **2018**, *126*, 88–98. [\[CrossRef\]](#)
72. Wang, W.; Yao, Q.; Tang, C.; Li, X.; Chong, Z.; Xu, Q. Experimental study on the shear characteristics and weakening mechanism of water-bearing rock joints. *Bull. Eng. Geol. Environ.* **2021**, *80*, 7653–7668. [\[CrossRef\]](#)
73. Lei, D.X.; Lin, H.; Chen, Y.F.; Cao, R.H.; Wen, Z.J. Effect of cyclic freezing–thawing on the shear mechanical characteristics of nonpersistent joints. *Adv. Mater. Sci. Eng.* **2019**, *2019*, 9867681. [\[CrossRef\]](#)
74. Li, B.; Ye, X.; Dou, Z.; Zhao, Z.; Li, Y.; Yang, Q. Shear strength of rock fractures under dry, surface wet and saturated conditions. *Rock Mech. Rock Eng.* **2020**, *53*, 2605–2622. [\[CrossRef\]](#)
75. Xie, S.; Han, Z.; Lin, H. A quantitative model considering crack closure effect of rock materials. *Int. J. Solids Struct.* **2022**, *251*, 111758. [\[CrossRef\]](#)
76. Basu, A.; Ram, B.K.; Nanda, N.K.; Nayak, S.S. Deterioration of shear strength parameters of limestone joints under simulated acid rain condition. *Int. J. Rock Mech. Min. Sci.* **2020**, *135*, 104508. [\[CrossRef\]](#)
77. Behnia, M.; Nateghpour, B.; Tavakoli, J.; Broujerdi, M.S. Comparison of experimental and empirical methods for estimating the shear strength of rock joints based on the statistical approach. *Environ. Earth Sci.* **2020**, *79*, 361. [\[CrossRef\]](#)